Extension of the Basin Rayleigh-Wave Amplification Theory to Include Basin-Edge Effects

Quentin Brissaud[*1], Daniel C. Bowden[2], and Victor C. Tsai[3]

ABSTRACT

The presence of sediments near the Earth's surface can significantly amplify the strength of shaking during earthquakes. Such basin or site amplification effects have been well documented in numerous regions, yet the complex and often situational dependence of competing reasons for this amplification makes it hard to quantify in a general sense or to determine the most significant contributions. Simple 1D seismic profiles can be used to estimate the amplitude differences between a basin site and a hard-rock reference site, but this ignores any reflections or conversions at the basin edge or a resonance effect depending on the basin's geometry. In this article, we explore an analytic model based on coupling coefficients for surface Rayleigh waves to account for the lateral discontinuities at a basin's edge (Datta 2018). We use this simple tool to explore the relationship between the basin's Rayleigh-wave amplification spectrum and various parameters such as basin depth, edge slope angle, and impedance contrast. The step-by-step construction of the model allows us to quantify the contributions from various wave propagation effects with the goal of identifying situations under which various basin-edge effects must be considered in addition to purely 1D estimates. For the most velocity contrasts (less than a factor of 5), the error made by the 1D theory in predicting maximum Rayleigh-wave basin amplification is under 35% for both the horizontal and the vertical components. For simple basins, the vertical amplification dominates at larger high frequencies and the horizontal at lower frequencies. Finally, we demonstrate from comparisons with spectral-element wavefield simulations that realistic velocity structures can be reduced to a simpler "box" shape for the semi-analytic formulation used here with reasonable results. For the purposes of estimating site-amplification or microzonation, an improved model that accounts for basin-edge effects can be implemented without high-computational cost.

KEY POINTS

- We explore analytically the link between the basin Rayleigh-wave amplification and basin properties.
- Although pure 1D theory provides reasonable estimates, higher-order mode conversion is a significant effect.
- The simple physics-based method we develop can provide better microzonation estimates than purely 1D models.

Supplemental Material

INTRODUCTION

Sedimentary basins cause significant amplification of seismic waves during earthquake shaking. This has been observed in many locations worldwide and has been the focus of many studies using empirical observations (Aki, 1993; Pratt *et al.*, 2003; Koketsu *et al.*, 2008; Marafi *et al.*, 2017), numerical simulation (Kawase, 1996; Olsen, 2000), analytic theory (Bard and Bouchon, 1985; Sánchez-Sesma and Velázquez, 1987; Bard *et al.*, 1988; Lontsi *et al.*, 2015), and every combination of approaches therein. Observations of higher amplitudes in basins are generally attributed to path or site effects, both of which are important for characterizing seismic hazard (Field, 2000; Borcherdt, 2014).

Amplification from site effects is often characterized by a 1D seismic velocity and density profile immediately beneath a given location. This usually assumes that strong shaking is dominated by vertically propagating shear waves that resonate

© Seismological Society of America

up and down in the flat shallow layers (Borcherdt, 2014). However, it is also well acknowledged that deeper structure and 3D shape of basins can play a significant role in further amplifying, focusing, or resonating particular frequencies (Bard and Bouchon, 1985; Field, 1996). Indeed, numerous studies have observed and remarked upon the importance of 3D basin effects, including works devoted to comparing the 1D to 3D estimates (Chavez-Garcia and Faccioli, 2000), to run simulations that account for complex basin shapes (Fäh et al., 1994; Graves et al., 2010), or to describe ray focusing using surface-wave travel-time derivatives (Dalton and Ekström, 2006; Lin et al., 2012). Despite such detailed efforts, it has remained difficult to quantify the importance of different effects in a general sense; the results of many such studies remain case-specific, and the relative importance of different effects can be difficult to quantify.

One potential improvement comes in acknowledging that the effect of 3D basins is different for different types of waves. Bowden and Tsai (2017) pointed out that the purely 1D amplification spectrum of surface waves will be different as compared to the vertically incident shear waves that are usually assumed. That is, in computing a frequency-dependent amplification between a hard-rock profile and a basin profile, the strength of amplification will be different depending on the wave type. Their theory assumes, however, as with the standard theory for vertically incident shear waves (Haskell, 1962), that all of the energy is transmitted from one site to another as the same mode and wave type, with no reflections, conversions, or any other competing 3D effect. These effects can be significant. For example, surface waves can be generated or amplified at basin edges (Hanks, 1975; Field, 1996; Kawase, 1996), surface waves can resonate laterally across a basin (Bard and Bouchon, 1985), higher-order modes of surface waves may dominate shaking for certain periods (Savage and Helmberger, 2004; Boué et al., 2016; Cruz-Atienza et al., 2016), or surface-wave energy can be focused by the basin-edge curvature (as in a lens, Feng and Ritzwoller, 2017). These phenomena are documented specifically for surface waves, but, again, most studies remain case-specific and are often difficult to compare.

The goal of this article is to expand on this purely 1D theory of Bowden and Tsai (2017) and account for transmission and reflection at the basin edges and wave interference within the basin. This is accomplished primarily by calculating the surface-wave's transmission and reflection coefficients, and consequently a term for mode conversion. This employs the software developed by Datta (2018) to compute these coefficients and semi-analytically derive the basin Rayleigh-wave amplification. The computation of transmission coefficients to approximate surface-wave Green's functions also bears similarity to work by Panza et al. (2001) for realistic basin hazard estimation, who describe a basin by a number of discretized boundaries in piecewise laterally homogeneous structures. The current study aims to expand on previous work by

performing numerical validation of transmission coefficients in basin structures and by considering reflections at lateral boundaries that are generally ignored.

This article remains focused on the effects of transduced Rayleigh waves, that is, Rayleigh waves generated by distant shallow earthquakes that are transmitted within the basin (Kawase, 2003). Future studies will include Love waves, which are an important contribution in the description of the basin response, but correspond to a different type of wave motion that requires an extended investigation. Whether Rayleigh waves contribute most strongly to seismic hazard depend on the earthquake source, the basin depth, and the frequency, or the type of measurement of interest; they may not play a strong role for high-frequency acceleration motions, but may be dominant when considering longer period displacements. The basins modeled here are intended to loosely represent possible scenarios at low frequency for the Los Angeles basin or the Mexico City basin (Field, 1996; Cruz-Atienza et al., 2016). The validation simulations (explained more later) include a point-source earthquake modeled directly at the Earth's surface, not because this is the most realistic, but because it will strongly generate surface waves for the purpose of this study.

The basins considered here are of a very simple geometry, as others have used (Narayan, 2010, 2012; Zhu et al., 2018). These simple models and the analytic formulation allow us to explore a range of scenarios and test the validity of various simplifying assumptions. By iteratively adding complexity to the models, we can understand the relative importance of different effects.

THEORY

In this section, we describe the surface-wave amplification between two geological sites as well as the expression of the surface-wave Green's function for a laterally heterogeneous medium. This will provide a framework for semi-analytically generating amplification spectra that we can later use to explore various basin effects.

1D amplification between two sites

In Bowden and Tsai (2017), the authors describe a 1D surface-wave amplification predictive model, based on the conservation of energy flux, building on the work of De Noyer (1961) and Tromp and Dahlen (1992). Given the 1D velocity and density profile at a reference site (denoted by superscript rock) and another site of interest, this ratio of amplitudes for the ith component and a given mode and surface-wave type is

$$\frac{A_i}{A_i^{\text{rock}}} = \frac{u_i(0)}{u_i^{\text{rock}}(0)} \left(\frac{UI_0}{U^{\text{rock}}I_0^{\text{rock}}} \right)^{-1/2}, \qquad (1)$$

in which A is the wave amplitude at the surface, $(u_i(0))_{i=1,2,3}$ is the displacement eigenfunction amplitude at the surface (in which $i = 1, 2$, or 3 for radial, vertical, and tangential

components of motion, respectively), U is the group velocity, and I_0 is an integral over the eigenfunctions and density such that

$$(\text{Rayleigh})I_0 = \int_0^\infty \rho(z)(u_1(z)^2 + u_2(z)^2)dz, (\text{Love})I_0$$
$$= \int_0^\infty \rho(z)u_3(z)^2 dz. \quad (2)$$

The primary assumption in equation (1) is that all of the surface-wave energy is transferred to within the basin, as the same wave type. This will only be the case if the change from one material to the other is relatively smooth, and no other 2D or 3D effects are significant. Therefore, it ignores a number of different wave propagation effects including: reflected energy away from the first basin edge, reflections and resonances within the basin, higher-order surface-wave modes and their interference, focusing or defocusing of surface-wave energy (as in a lens), and body-wave conversions. We note that lateral surface-wave reflections and resonances within the basin are qualitatively similar to the vertical resonances observed in a sediment column for vertically propagating *SH* waves. Other than focusing and body-wave conversions, all of the other effects listed will be investigated in this article.

Adding a basin edge

Generally, lateral variations of seismic velocities may not be smooth. Whether a velocity contrast may be considered sharp and significant depends on the horizontal gradient relative to the wavelength of interest, specifically:

$$\frac{|\nabla_x V_P|}{V_P} \ll \frac{\omega}{c(\omega)}, \frac{|\nabla_x V_S|}{V_S} \ll \frac{\omega}{c(\omega)}, \frac{|\nabla_x \rho|}{\rho} \ll \frac{\omega}{c(\omega)}, \quad (3)$$

in which ∇_x is the horizontal gradient operator. We note that while the change from sediments to hard rock is itself almost always a sharp geologic boundary, for surface waves, a gently sloping basin edge may be considered to be a smooth lateral boundary (Keilis-Borok, 1989).

Because real sedimentary basins have complex geometries and highly heterogeneous velocity structures, we have to make some simplifications to be able to perform an analytic study of the seismic amplification. Figure 1 shows the typical basin structure that we will consider in this article. As will be described in the next section, this allows us to write surface-wave transmission and reflection coefficients at the basin edges and better describe the energy distribution across the basin.

The structure corresponds to an axisymmetric basin (2.5-d) defined by its length L_{basin}, depth h_{basin}, basin-edge slope γ, and two different seismic velocities and densities. These basin parameters are the most significant for constraining the amplification within the basin (Narayan, 2010, 2012; Moczo *et al.*,
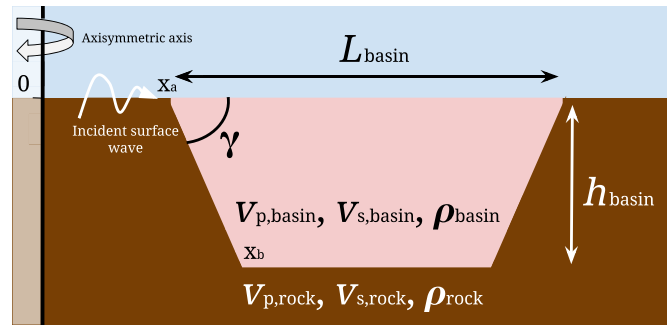

Figure 1. Geometry of the basin used for simulations. γ is the basin-edge angle (rad), L_{basin}, h (km) are the basin length and depth, respectively, V_P (km s^{-1}) is the compressional velocity, V_S (km s^{-1}) is the shear velocity, and ρ (kg m^{-3}) is the density. The subscript basin and rock correspond, respectively, to the basin and the rock-site properties. $\mathbf{x}_a$ is the location of the basin edge at the surface and $\mathbf{x}_b$ its location at depth. The color version of this figure is available only in the electronic edition.

2018). At first we consider homogeneous blocks of seismic structure as in Figure 1, and later we also explore a 1D stratified velocity structure according to an increasing power-law model $V_{S,\text{basin}} = V_{0,\text{basin}}(z)^{\alpha_{\text{basin}}}$ to investigate the impact of stratification.

Similarly, for much of the article we will use an even more severe simplification of a box shape for which the basin edge is perfectly vertical ($\gamma = \pi/2$). This may be considered a "worst-case" scenario in regards to the applicability of a purely 1D theory, because the vertical, sharp boundary will have a stronger effect on propagating waves. Specifically, exploring a range of best-case or worst-case scenarios in regards to the importance of various effects will be the focus of a later section.

Surface-wave propagation and transmission within a basin

To account for transmission at the first basin edge, reflections within the basin, dispersion, and attenuation, we describe here the expression for Green's functions describing the propagation across a vertical boundary. This boundary can be described in terms of propagation and reflection coefficients, but specifically coefficients exist for a given mode's intra- and intercoupling. For example, the fundamental mode surface wave will not only reflect and transmit as a fundamental mode (intracoupling), but will also reflect and transmit some amount of energy into higher-order modes as well (intercoupling).

For simplicity, in this section, we only consider a homogeneous hard-rock reference with, therefore, only one incident fundamental Rayleigh-wave mode. Our notation is as follows: at the first basin edge, the incident fundamental-mode propagating in the rock is transmitted into various other possible modes $n = 0, N_m$ with amplitude $T_{i,(n)}$ that will propagate within the basin. Then, as waves reflect on the far basin edge,

they may be converted into waves of mode $m = 0, N_m$, with amplitude $R_{i,(m)}^{N_r}$, in which the superscript N_r corresponds to the total number of reflections within the basin. The reflected energy after one reflection will then be reflected and converted again on the first basin edge. For simplicity, we denote by $R_{i,(m)}^{N_r}$ the entirety of the reflected wavefield after N_r reflections due to an incident mode (m). These coefficients, $(T_{i,(n)}, R_{i,(m)}^{N_r})_{n,m=0,N_m}$, include the energy converted between different modes (i.e., intercoupling coefficients) that is a primary difference between the method used here and the purely 1D theory from the previous section. These intercoupling coefficients are known to be significant for surface-wave propagation across strong lateral heterogeneities (Maupin and Kennett, 1987). Coefficients $(T_{i,(n)}$ and $R_{i,(m)}^{N_r})_{n,m=0,N_m}$ are surface displacement ratio of, respectively, transmitted and reflected to incident waves (Datta, 2018). We refer to $(T_{i,(n)}$ and $R_{i,(m)}^{N_r})_{n,m=0,N_m}$ as transmission and reflection coefficients in the rest of the article for simplicity.

In this configuration, the amplitude A_i of the ith component motion of the surface-wave train composed of N_m modes within the basin is

$$A_i(f, x; L) = S_j(f) | \sum_{n=0}^{N_m} G_{(0),ij}^{\text{rock}}(f, x = \mathbf{x}_a) T_{i,(n)}(f, x) R_{i,(n)}^{N_r}(f, x)|, \tag{4}$$

in which $(S_j)_{j=1,3}$ is the source frequency spectrum for the jth component, $(G_{(0),ij}^{\text{rock}})_{i,j=1,3}$ are the components of the rock-site fundamental-mode Green's functions, N_m is the number of modes propagating within the basin, and N_r is the number of reflections within the basin. $T_{i,(n)}$ corresponds to the ith transmitted energy of mode n, whereas $R_{i,(n)}^{N_r}(f, x)$ is the reflected energy after N_r reflections at a location x within the basin due to the incident surface-wave mode n; these are defined more fully in the supplemental material along with the full solution for heterogeneous rock sites. Taking the ratio of basin-to-rock surface-wave amplitude using equation (4), the amplification spectrum reads:

$$\frac{A_i(f, x)}{A_i^R(f, x)} = \frac{| \sum_{n=0}^{N_m} G_{(0),ij}^{\text{rock}}(f, x = \mathbf{x}_a) T_{i,(n)}(f, x) R_{(n)}^{N_r}(f, x)|}{| \sum_{l=0}^{N_{m,\text{rock}}} G_{(l),ij}^{\text{rock}}(f, x)|}. \tag{5}$$

The expression (5) enables us to analytically study the influence of basin structure on surface-wave propagation. It also greatly simplifies the study of higher-order mode conversions and resonances in the basin, because we can directly identify the contributing factors in the amplification spectrum through the surface-wave Green's function expression.

The coefficients $(T_{i,(n)})_{n=1,N_m}$ and $(R_{i,(m)})_{m=1,N_m}$ can be analytically determined using theory for surface-wave propagation through a plane vertical interface (Alsop *et al.*, 1974; Malischewsky, 1976; Its and Yanovskaya, 1985; Maupin and Kennett, 1987; Marquering and Snieder, 1995; Romanelli *et al.*,

1997). Vertical boundaries enable one to express the surface-wave field in terms of incident, reflected, and transmitted waves. Details about the theoretical framework can be found in Keilis-Borok (1989, his chapter 3.3). The coefficients $(R_{(m)})_{m=1,N_m}$ correspond to reflections occurring within the basin and not from the rock to the basin, because the latter is implicitly accounted for in the transmission coefficients $(T_{(n)})_{n=1,N_m}$.

To solve the transmission-and-reflection problem at the boundary (equations 3.8 and 3.9 in Keilis-Borok, 1989), we use the implementation of Datta (2018) based on the Rayleigh-wave theory by Its and Yanovskaya (1985). However, the initial implementation for Rayleigh waves by Datta (2018) only focused on the vertical component, we, therefore, extended his work by implementing the horizontal component in the same framework. There are four main assumptions behind the calculation of those coefficients: (1) the coefficients are valid in the far field of the basin edge, (2) the wave incidence is assumed orthogonal (i.e., there are no Rayleigh-to-Love wave conversions), (3) the diffraction of body waves at the interface is negligible, and (4) the interface is assumed to be vertical. This assumption can be partially relaxed as Its and Yanovskaya (1985) extended the theory to inclined interfaces for incident wavelengths λ_0 larger than the distance between the slope extremities ($\mathbf{x}_a$ and $\mathbf{x}_b$) such that $\lambda_0 >> \frac{h_{\text{basin}}}{\tan \gamma}$ (Its and Yanovskaya, 1985). For the sake of providing a complete description of 2D basin effects, in the current article, we will later investigate numerically the impact of angles γ on the amplification.

Although equation (5) is valid for both Love and Rayleigh waves, we explore basin effects for Rayleigh waves only in this article for clarity. Nonetheless, we note that the methodology would be very similar for Love waves and will be the focus of future work.

Numerical method to generate reference amplification spectra

Finally, to compute reference amplification spectra and provide meaningful comparisons with the theoretical model previously described, we compute higher-order numerical solutions. The numerical method employed in this article is the axisymmetric version of the seismic wave propagation package SPECtral Finite EleMents (SPECFEM) (Komatitsch and Vilotte, 1998), which is based on a weak Galerkin formulation with spectral finite elements and Gauss–Lobatto–Legendre points. SPECFEM accounts for complex velocity structures and attenuation. To generate a wavefield dominated by surface waves, we use a vertical point force at the surface located at least three times the Rayleigh-wave wavelength away from the basin edge. In an elastic, homogeneous, and isotropic medium, locating the source three times the wavelengths from the basin edge ensures that the body-wave contribution is negligible (Tamura, 1996). The vertical point force follows a

Gaussian time function with half-duration $t_0 = 1/f_0 = 1/(f_h \approx \frac{v_{s,\text{basin}}}{2.25 h_{\text{basin}}})$ s, in which f_0 is the dominant frequency in the basin (described in detail in the next section). To ensure that the Rayleigh-wave propagation is not altered by the domain geometry, we choose a basin edge located in the source far field, and we extend the mesh vertically until the displacement eigenfunctions are of amplitude <0.01 at the source dominant frequency. Finally, we apply absorbing boundary conditions on each side of the domain to avoid spurious numerical reflections. The spectral amplification is then computed by taking, for a given location, the ratio of the Fourier transform of the velocity waveform from a numerical simulation, including a basin, and from a separate numerical simulation where the basin did not exist.

INFLUENCE OF BASIN STRUCTURES ON SURFACE-WAVE PROPAGATION

To study the influence of basin structures on the amplification spectrum in sedimentary basins, we will consider various basin configurations with increasing complexity. By successively adding complexity, and by controlling which terms in our Green's Function formulation are used, we can explore the impact of different effects independently. Five main features will be discussed in the following sections: transmission and reflection coefficients of the incoming surface wave in the Basin-edge velocity contrast and mode conversion section, attenuation in the Attenuation section, stratified layers instead of homogeneous blocks in the Stratification section, lateral resonance in the Lateral resonance section, and the slope of the basin edge in the Edge slope section.

Throughout this section, we generally focus on variations in shear-wave velocity and use empirical relations between density to V_P and V_P to V_S, as in equations (1) and (9) in Brocher (2005) (this will be relaxed in later sections). To provide generic results, we use a normalized frequency f/f_h, in which the dominant vertical amplification frequency f_h depends upon the basin characteristics. Narayan (2010) empirically observed that this f_h relates to basin depth h_{basin} and shear-wave velocity $V_{S,\text{basin}}$ as

$$f_h \approx \frac{V_{S,\text{basin}}}{2.25 h_{\text{basin}}}. \tag{6}$$

The empirical formula (6) has been tested against numerical results in the supplemental material. We point out that equation (6) differs from the traditional S-wave resonant frequency $f_{h,S\text{ wave}} = \frac{V_{S,\text{basin}}}{4 h_{\text{basin}}}$. Although the dominant frequency might slightly differ from equation (6) for the horizontal fundamental-mode Rayleigh wave, in this section, for consistency, we will only show the spectra in terms of normalized frequency based on the vertical component.

Although the notion of dominant frequency in equation (6) is poorly constrained for basins with strong lateral

inhomogeneities and shear-wave velocity variations with depth, using a normalized frequency enables us to generalize the results for simple basin structures. Not only does the dominant frequency correlate with the basin depth and the basin shear-wave velocity, but also more importantly the spectrum scales with the basin depth for a given velocity model (Brissaud and Tsai, 2019). More specifically, if we consider two basins defined by the same velocity model and basin depths h_1 for the first basin and $h_2 = \alpha h_1$ for the second basin, amplification spectra defined by equation (4) for media 1 and 2 read

$$\frac{A_i^1(f, x)}{A_i^{1,R}(f, x)} = \frac{A_i^2(f\alpha, x\alpha)}{A_i^{2,R}(f\alpha, x\alpha)}, \tag{7}$$

in which the superscripts 1, 2 denote the media 1 or 2, respectively.

Basin-edge velocity contrast and mode conversion

We first use our analytic framework described in equation (5) to explore the effect of transmission coefficients and mode conversions, as compared to the purely 1D theory and compared to the fully numerical SPECFEM solution.

Numerous studies show that the velocity contrast at the basin bottom has a strong impact on the maximum amplitude and dominant frequency of the amplification spectrum (Bard and Bouchon, 1985; Meier and Malischewsky, 2000; Tuan *et al.*, 2011; Narayan, 2012; Moczo *et al.*, 2018). In addition to the transmission and reflection of the fundamental-mode Rayleigh wave, energy conversion to higher modes occurs at sharp boundaries. Those higher-order surface-wave modes propagate in the basin and can constructively and destructively interfere with the fundamental mode (Savage and Helmberger, 2004; Boué *et al.*, 2016).

We first consider a 1 km deep basin, with only a vertical velocity contrast on one side (the other edge may be thought of as infinitely far away). The rock shear-wave velocity is assumed to be 2 km/s and the basin sediments to be either 1.2 or 1.4 km/s. Comparisons are presented in Figure 2, with amplification curves from a purely 1D theory for fundamental Rayleigh-wave amplification, our improved semi-analytic theory, which accounts for basin-edge effects, and the true solution ("num. simulation"). The purely 1D theory result in Figure 2a shows a typical example of an amplification spectrum in a sedimentary basin that can be divided into three frequency domains: an unamplified low-frequency part for $f/f_h \ll 1$, which corresponds to the solution for a thin basin layer (Malischewsky, 1976, his chapter 2.1.2), a dominant peak for $f/f_h \approx 1$ due to the discontinuity in the seismic velocity model, and a high-frequency part for $f/f_h \gg 1$ that converges to the value given by the quarter-space approximation (equation 2.13 in Clement, 1961). The purely 1D theory tends to overpredict the amplification amplitude throughout the spectrum, because this neglects effects at the basin edge.
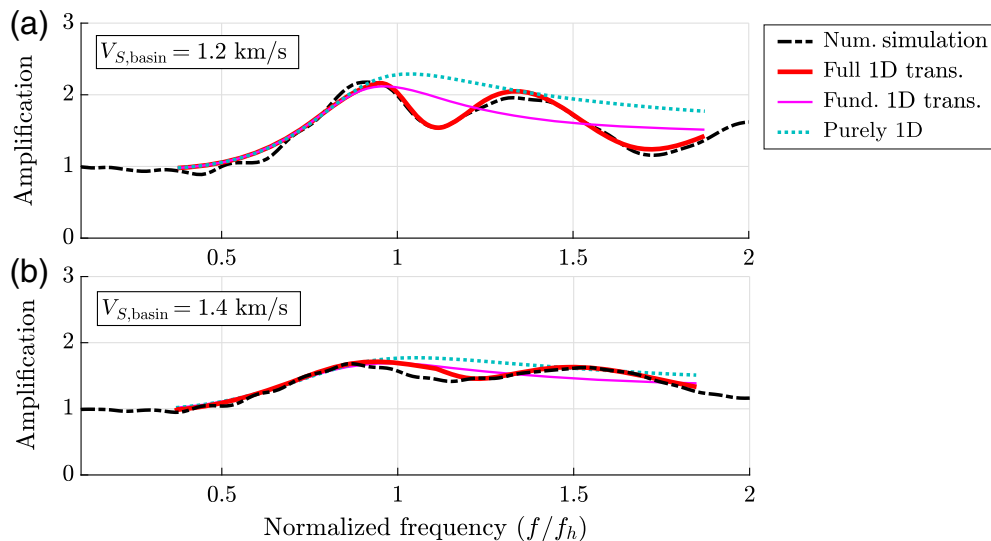
Figure 2. Vertical amplification spectrum against normalized frequency from numerical simulation ("num. simulation," black dashed line), from the 1D transmission coefficients for the fundamental and first higher-order mode ("full 1D trans." thick red line), from the 1D transmission coefficients for the fundamental mode only ("fund. 1D trans." pink line), and from the purely 1D theory ("purely 1D," blue dashed line) at distance $x = 5$ km from the basin edge, for (a) $h_{basin} = 1$ km, $V_{0,basin} = 1.2$, and $V_{0,rock} = 2$ and for (b) $V_{0,basin} = 1.4$ km/s and $V_{0,rock} = 2$ km/s. The color version of this figure is available only in the electronic edition.
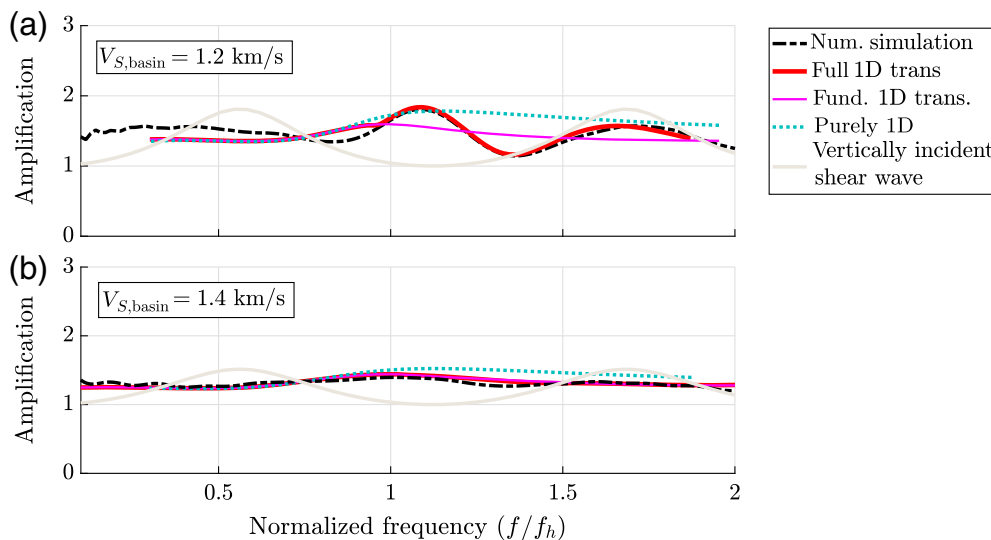

Figure 3. Horizontal amplification spectrum against normalized frequency from numerical simulation ("num. simulation," black dashed line), from the 1D transmission coefficients for the fundamental and first higher-order mode ("full 1D trans." thick red line), from the 1D transmission coefficients for the fundamental mode only ("fund. 1D trans." pink line), from the purely 1D theory ("purely 1D"), and from a vertically incident shear wave ("vertically incident shear wave," gray line) at distance $x = 5$ km from the basin edge, for $h_{basin} = 1$ km and $V_{0,rock} = 2$ for (a) $V_{0,basin} = 1.2$ and (b) $V_{0,basin} = 1.4$. The color version of this figure is available only in the electronic edition.

constructive or destructive interference introduces periodicity in the time series and, therefore, extra peaks and troughs in the energy spectrum. Particle motions associated with Figure 2a,b are provided in the supplemental material showing a prograde first higher-order mode propagates faster than a retrograde fundamental mode. Thus, we already see the advantage of estimating reflection and transmission coefficients and consequently the higher-order mode conversions. The red lines ("full 1D trans") match the numerical simulations (black dashed lines) remarkably well, suggesting that the analytic approximations described in equation (4) is quite sufficient for this model. Around $f/f_h \approx 1.15$, we observe a small discontinuity in the amplification spectrum in Figure 2b. This jump can be attributed to the rapid amplitude increase around $f/f_h \approx 1.15$ of the first-order transmission coefficient that is zero for $f/f_h < 1.15$. Later sections, as well as the supplemental material, further compare the various approaches in terms of spatial location in the basin, maximum amplification, and frequency of maximum amplification.

We also show in Figure 3 the amplification spectrum for the horizontal component of motion. By comparing Figures 2a and 3a, we observe that for the amplifications of the fundamental-mode Rayleigh waves, the horizontal and vertical amplification spectra are somewhat similar in terms of dominant frequency and maximum amplification. This might be expected as horizontal and vertical eigenfunctions are affected by the basin discontinuity in a similar manner. However, some differences do

Comparing Figure 2a and b, we note that the higher the velocity contrast, the larger the discrepancy between the true solution and the purely 1D theory. Because higher-order mode Rayleigh waves propagate with different velocities, their

remain: whereas the vertical amplification is generally larger at higher frequencies $f > 0.75f_h$, at lower frequencies of $f < 0.75f_h$ the horizontal amplification dominates. The differences are more significant when including the fundamental-to-first-mode transmission coefficient. In Figure 3a, comparing the horizontal and vertical full 1D transmission coefficients, we observe constructive interference between the modes shifts the horizontal amplification's maximum toward higher frequencies, which corresponds to a "trough" in the vertical amplification spectrum. The horizontal and vertical spectra tend to be "out-of-phase", that is, a local maximum for the vertical component corresponds to a local minimum for the horizontal component and vice versa, for $f > 0.75f_h$. The spatial dependence of this "out-of-phase" behavior is further explored in the supplemental material. At lower frequencies, we observe discrepancies between the semi-analytical and the numerical solutions that we think are due to the stronger Rayleigh-to-body wave diffraction at the basin edge (not taken into account by the analytical model) for the horizontal component than for the vertical component. Finally, for a lower velocity contrast, shown in Figure 3b, the influence of higher-order modes tend to be less significant for the horizontal component than for the vertical component, and the horizontal amplification spectrum converges to the fundamental-mode transmission coefficient. Figures 2 and 3 show results for one location only, but similar observations can be made further away from the basin edge. We provide additional details about the spatial dependence of the wavefield within the basin in the supplementary material.

Because the difference between the horizontal and the vertical surface-wave amplifications will be similar for many of the basin effects investigated in the rest of the section, for conciseness, we will only show the horizontal component when the horizontal spectra show unique features. We emphasize that for surface waves the horizontal and vertical components are very often similar, and so any general patterns or behaviors observed here may be considered applicable to both components of motion unless stated otherwise. We also remind the reader that the curves described here are for amplification, not absolute amplitudes themselves. At a hard-rock site, Rayleigh-wave horizontal-to-vertical ratios are typically less than one, meaning the absolute horizontal amplitudes are smaller to begin with. Therefore, the absolute horizontal amplitude within a basin can theoretically be smaller than the absolute vertical amplitude.

Finally, we note that vertically incident SH body waves exhibit a periodicity in the amplification spectrum from resonance overtones (Thompson $et\ al.$, 2009). In a simple homogeneous basin, the maximum shear-wave amplification occurs around multiples of $f = \frac{V_S}{4h_{\text{basin}}} \approx 0.56f_h$, meaning that a minimum is reached at $f = 1.12f_h$, approximately when the Rayleigh-wave amplification comes to a maximum, which can potentially lead to the misinterpretation of the observed

signal. We note that we include the amplification of vertically incident shear waves here for comparison, but remind the reader that the numerical simulations (black dashed curves) are designed to be shallow and thus excite strong surface waves; a different simulation would be needed to further comment on the 2D or 3D amplification effects of body waves.

Besides mode conversions, reflections also occur at the basin edge, and, energy is partially reflected back to the rock, effectively lowering the observed amplitudes in the basin. In Figure 4, we show both the transmission and the reflection coefficients against normalized frequency for various velocity contrasts as well as the maximum value of both the transmission and reflection coefficient in the range of normalized frequency $f/f_h = [0.4; 3]$. The reflection coefficient is not component dependent, because we consider in this section that only the fundamental mode can propagate outside of the basin. These reflection coefficients correspond to a wave propagating in the rock and are being reflected at the basin edge and not within the basin. By comparing Figure 4b,d,e, we observe that the higher the velocity ratio, the larger the transmission not only for both the components but also the reflection. The local reflection maximum around $f/f_h \approx 1$ also corresponds to the amplification peak and has large values for large velocity ratios that can no longer be neglected when computing the amplification within the basin. This normalized frequency $f/f_h \approx 1$ and the corresponding amplitude of the reflection are important values that have been used in the past to locate and measure discontinuity depths (e.g., Meier $et\ al.$, 1997; Meier and Malischewsky, 2000; Du, 2002). Figure 4f relates to the percentage of inaccuracy in maximum amplification of the purely 1D theory for a given velocity contrast, because the 1D theory does not account for reflections (see the Accuracy of the 1D Theory for Maximum Amplification Predictions section for more details).

Attenuation

Attenuation will also play an important role in the energy distribution, as typical sedimentary basins generally have low-quality factors (Hauksson $et\ al.$, 1987; Hauksson and Shearer, 2006). A frequency-dependent quality factor can be taken into account in equation (5) through the Green's functions exponential damping term in equation (5) (more details are provided in the supplementary material). To illustrate the impact of attenuation on the amplification spectrum, we compare unattenuated propagation with propagation for a simple basin attenuation model $Q_s = 5\% V_{S,\text{basin}}$, with $V_{S,\text{basin}}$ in meters per second, and $Q_p = 2Q_s$ (Graves and Pitarka, 2010). The Rayleigh-wave quality factor can be simply computed from Q_p, Q_s and the Rayleigh-wave phase velocity (Anderson $et\ al.$, 1965). Amplification spectra are shown in Figure 5a,c,d, in which we observe that attenuation lowers the amplification and eventually reaches values <1 for some frequencies at large distances from the basin edge. In
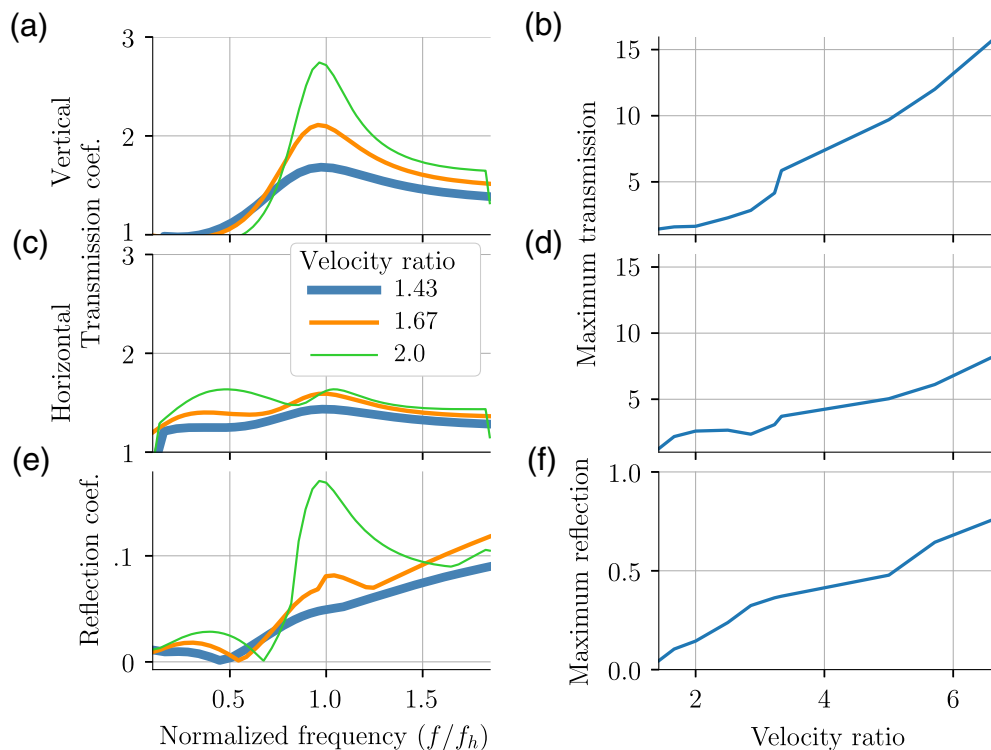
Figure 4. (a) Fundamental-mode vertical transmission coefficients against normalized frequency, (b) maximum amplitude of the fundamental-mode vertical transmission coefficients in the range of normalized frequency $f/f_h = [0.4; 3]$ against rock-to-basin shear-velocity ratio, (c) fundamental-mode horizontal transmission coefficients against normalized frequency, (d) maximum amplitude of the fundamental-mode horizontal transmission coefficients in the range of normalized frequency $f/f_h = [0.4; 3]$ against rock-to-basin shear-velocity ratio, (e) fundamental-mode reflection coefficients against normalized frequency, and (f) maximum amplitude of the fundamental-mode reflection coefficients in the range of normalized frequency $f/f_h = [0.4; 3]$ against rock-to-basin shear-velocity ratio. (a,c,e) Show coefficients for various rock-to-basin shear-velocity ratios $V_{S,\text{rock}}/V_{S,\text{basin}} = 1.43$ (thick blue line, corresponding to Fig. 3a), 1.67 (orange line, corresponding to Fig. 3b), and 2 (thin green line). The reflection coefficient is not component dependent because we consider that only the fundamental mode can propagate outside of the basin in the Basin-edge velocity contrast and mode conversion section. The color version of this figure is available only in the electronic edition.

Figure 5b, the fundamental mode has lower Q values than the first higher-order mode. Because the sensitivity of higher-order modes penetrates to larger depths than the fundamental mode for any given frequency, the fundamental mode will be more sensitive to the shallow surface, where attenuation is usually stronger, and therefore more dampened than the higher-order modes. Around $f/f_h \approx 1$, we observe a small discontinuity in the amplification spectrum. Similar to Figure 2b (around $f/f_h \approx 1.15$), this jump can be attributed to the rapid amplitude increase around $f/f_h \approx 1$ of the first-order transmission coefficient that is zero for $f/f_h < 1$. As was the case with Figure 2, we emphasize that our semi-analytic formulation ("full 1D trans.", thick red line) matches the numerical simulation (black dashed line) rather well. Attenuation in the rock can also be taken into account by introducing the corresponding shear-wave quality factor in the rock-site Green's function in equation (5).

Stratification

So far we have considered simple homogeneous basin- and rock-site velocity models. However, a more realistic approximation consists of using power-law shear-velocity structures to describe the subsurface (Boore and Joyner, 1997). Basin shear-wave velocity layering is known to have an impact on the fundamental frequency, the maximum amplification, and the dispersion of surface waves (Narayan and Singh, 2006). In this section, we consider a power-law shear-velocity structure (defined by parameters $h_{\text{basin}} = 1$ km, $\alpha_{\text{basin}} = 0.1$, $V_{0,\text{basin}} = 1.2$ km/s, and $V_{0,\text{rock}} = 2$ km/s) along with a strong discontinuity at the sediment-rock bottom boundary. Because a pure power law leads to a zero velocity at the surface that is unphysical and numerically unstable, we consider the shear velocity to be constant for depths $z < 0.01$ m, corresponding to a minimum velocity of 0.380 km/s. The velocity model for the rock site, and the basin structure is shown in Figure 6b.

Amplification spectra are shown in Figure 6a,c. We observe that the complex amplification pattern produced by the soil layering is accurately captured by the transmission coefficients. The maximum amplification peak in Figure 6a is modestly underpredicted by the purely 1D theory due to the constructive interference of higher-order modes with the fundamental mode. Because of the highly dispersive nature of surface waves in layered media, several amplification peaks appear in Figure 6c with roughly similar amplitudes. Those high-amplitude amplification peaks show the importance of considering higher-order modes to fully constrain the amplification spectrum.

Lateral resonance

Our models up to this point have only considered the basin edge for which surface waves enter the basin, but lateral boundaries will reflect waves back and forth within the basin and eventually constructively and destructively interfere
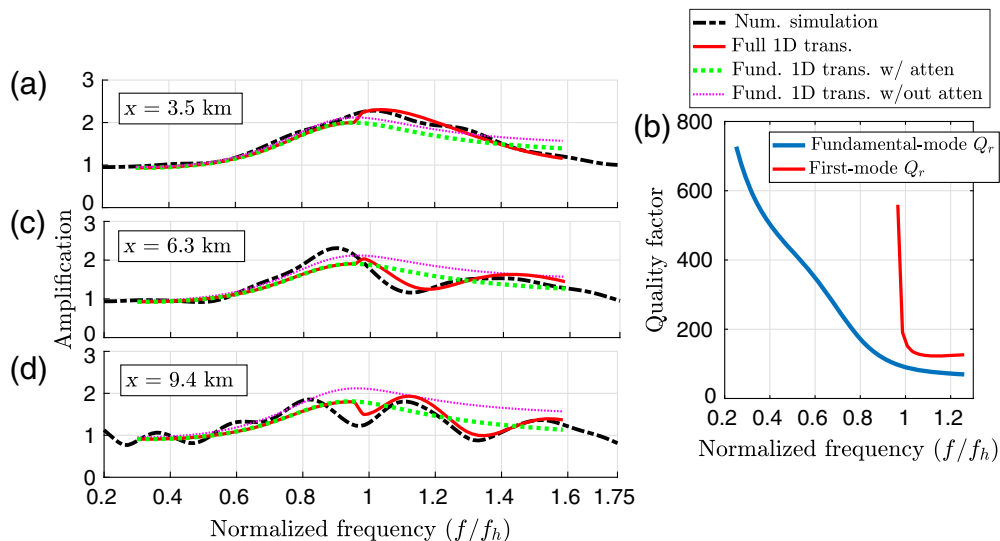
Figure 5. Vertical amplification spectrum against normalized frequency from numerical simulation ("num. simulation," black dashed line), from the 1D transmission coefficients for the fundamental and first higher-order mode ("full 1D trans." thick red line), from the 1D transmission coefficients for the fundamental-mode only ("fund. 1D trans." pink dashed line) and from the 1D transmission coefficients for the fundamental-mode only without attenuation ("fund. 1D trans. without attenuation," thick dashed green line) at distance (a) $x = 3.5$ km, (c) $x = 6.3$ km, and (d) $x = 9.4$ km from the basin edge, for $h_{basin} = 1$ km, $V_{0,basin} = 1.2$ km/s, and $V_{0,rock} = 2$ km/s with shear-wave quality factor $Q_S = 0.05 V_{S,basin}$ and $Q_P = 2Q_S$. (b) Rayleigh-wave quality factor against normalized frequency for the fundamental mode (blue) and the first higher-order mode (red). The color version of this figure is available only in the electronic edition.
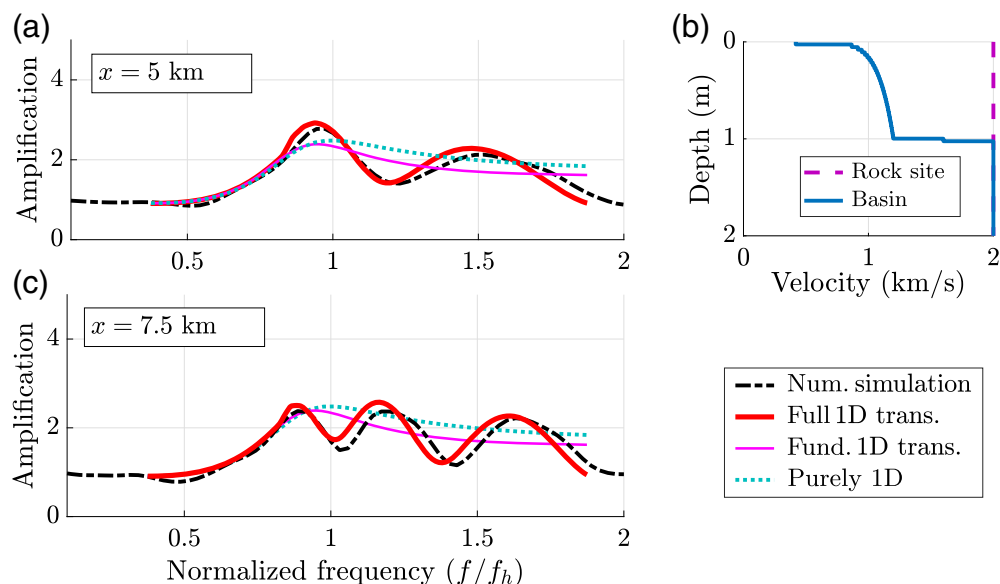

Figure 6. Vertical amplification spectrum against normalized frequency from numerical simulation ("num. Simulation," black dashed line), from the 1D transmission coefficients for the fundamental and first higher-order mode ("full 1D trans." thick red line), from the 1D transmission coefficients for the fundamental mode only ("fund. 1D trans." pink line), and from the purely 1D theory ("purely 1D," dashed blue) at distance (a) $x = 5$ km and (c) $x = 7.5$ km from the basin edge, for $h_{basin} = 1$ km, $\alpha_{basin} = 0.1$, $V_{0,basin} = 1.2$ km/s, and $V_{0,rock} = 2$ km/s. (b) Shear-wave velocity model against depth for the rock site (pink dashed line) and the basin (blue line). The color version of this figure is available only in the electronic edition.

(Sanchez-Sesma and Luzon, 1995; Narayan, 2005). To compute the effect of lateral resonance within a basin, following equation (5), we can also consider the reflection coefficients at the opposing basin edge.

Amplification spectra for various basin lengths L_{basin} are shown in Figure 7, stated in terms of the basin-shape ratio. We observe that as the basin-shape ratio decreases, the spectral oscillations widen as the arrival time of reflections gets closer to the arrival time of the incident wave. The spatial and frequency dependence of the interference between incident and reflected wavefields are further explored in the supplementary material.

We note that Liu and Zhou (2016) showed that the near-field Rayleigh waves tend to have lower amplitudes and later arrivals than far-field Rayleigh waves. Therefore, in the current analytic framework, the predicted spectra provide an upper bound for maximum amplification in basin structures showing lateral resonances. Additional details about the near-field and far-field discrepancies are given in the supplementary material.

Rather than continue to focus only on specific basin examples, the semi-analytic form developed in equation (5) can quickly generate amplification spectra for any basin length L_{basin} and at any location x within the basin. In Figure 8, we show the maximum amplification (see Fig. 8b,d, as well as the corresponding frequency of that maximum, see Fig. 8a,c) against relative location in the
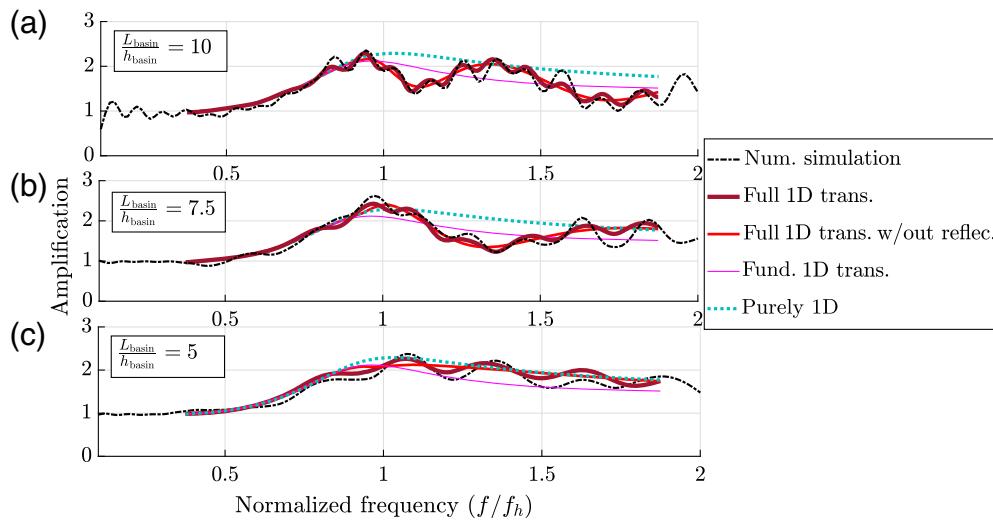
Figure 7. Vertical amplification spectrum against normalized frequency from numerical simulation ("num. simulation," black dashed line), from the 1D transmission and reflection coefficients for the fundamental and first higher-order mode ("full 1D trans." dark thick red line), from the 1D transmission coefficients for the fundamental and first higher-order mode ("full 1D trans. without reflection," light red line), from the 1D transmission coefficients for the fundamental mode only ("fund. 1D trans." pink line), and from the purely 1D theory ("purely 1D," blue dashed line) at the center of the basin, for (a) $L_{\text{basin}} = 10$ km, for (b) $L_{\text{basin}} = 7.5$ km, and for (c) $L_{\text{basin}} = 5$ km with $h_{\text{basin}} = 1$ km, $V_{0,\text{basin}} = 1.2$ km/s, and $V_{0,\text{rock}} = 2$ km/s. $L_{\text{basin}}/h_{\text{basin}}$ is the basin-shape ratio. The color version of this figure is available only in the electronic edition.

basin and basin-shape ratio for two test cases: by neglecting lateral resonance (see Fig. 8a,b, and by including lateral resonance, see Fig. 8c,d). When neglecting reflections, variations in amplitude for increasing basin-shape ratios are a result of the nondimensionalization of the location in the basin using the basin length. By taking into account of reflections within the basin, the maximum amplification is increased by approximately 8%, for this given velocity contrast, due to the constructive interference between incoming and reflected waves from various modes. Lateral resonance also changes the location of the global maximum (blue dots in Fig. 8b,c) toward larger basin-shape ratios and brings it closer to the right edge of the basin. We note that the location of maximum interference is affected by both geometrical attenuation and wave-train dispersion. The strongest interference here occurs close to the right-side basin edge (for $x/L_{\text{basin}} > 0.6$), because this is the first place the two wave trains meet, and after this the waves are only further damped by geometrical effects. Especially for large basin-shape ratios ($L_{\text{basin}}/h_{\text{basin}} > 30$) and for locations $x/L_{\text{basin}} > 0.6$, the complex interactions between the various incoming and reflected Rayleigh-wave modes strongly alter the maximum amplification. For basin-shape ratios $L_{\text{basin}}/h_{\text{basin}} < 30$, we observe more distinct peaks and troughs in maximum amplification against relative location when including reflections (Fig. 8d) than when ignoring reflections (Fig. 8b). Taking into account, reflections leads to destructive interference between incoming and reflected modes, depending on the location within the basin. Not only the

amplification's maximum is affected but also its dominant frequency, as shown in Figure 8c, in which for locations $x/L_{\text{basin}} > 0.7$, the maximum is shifted toward higher frequencies, such that $f/f_h > 1$, due to the constructive interference of higher-order modes.

As mentioned in the Basin-edge velocity contrast and mode conversion section, the velocity contrast has a strong effect on the maximum amplification. In Figure 9, we show the maximum amplification against basin-shape ratio and relative location for $\frac{V_{S,\text{rock}}}{V_{S,\text{basin}}} = 2$. We observe in Figure 9b that a larger velocity contrast leads to a larger maximum amplification. Because a larger shear-wave velocity contrast leads to the propagation of more dispersive higher-order modes, constructive interference occurs throughout the basin, and the peak of maximum amplification against location broadens. Moreover, the lower shear-wave velocity in the basin makes the maximum for a given basin-shape ratio occur farther from the left edge. Horizontal motions show similar patterns and are shown in the supplementary material.

When neglecting attenuation, we observe strong interference between surface-wave modes throughout the basin for large basin-shape ratios. However, when including strong attenuation, we expect the waves travelling long distances to be greatly attenuated. In Figure 10a,b, we show the same maps as in Figure 8c,d, but including a low-shear-wave quality factor such that $Q_s = 5\% V_{S,\text{basin}}$, with $V_{S,\text{basin}}$ in meters per second, and $Q_p = 2Q_s$ (as in the Attenuation section). We observe that for low basin-shape ratios ($L_{\text{basin}}/h_{\text{basin}} < 30$) or locations close to the left edge ($x/L_{\text{basin}} < 0.3$) the map of maximum amplification in an anelastic basin in Figure 10b, while having lower amplitudes (global maximum ≈8% lower than in the elastic case), shows similar trends compared to the elastic case because waves have not travelled long distances. However, for $L_{\text{basin}}/h_{\text{basin}} > 30$ and $x/L_{\text{basin}} > 0.3$ we mainly observe the first transmitted Rayleigh waves, as in Figure 8b. Reflections do not lead to strong interference anymore, because they have been strongly attenuated, especially for large basin-shape ratio. Moreover, attenuation leads to significantly lower frequencies at maximum amplification, because most of the higher frequency energy has been damped.
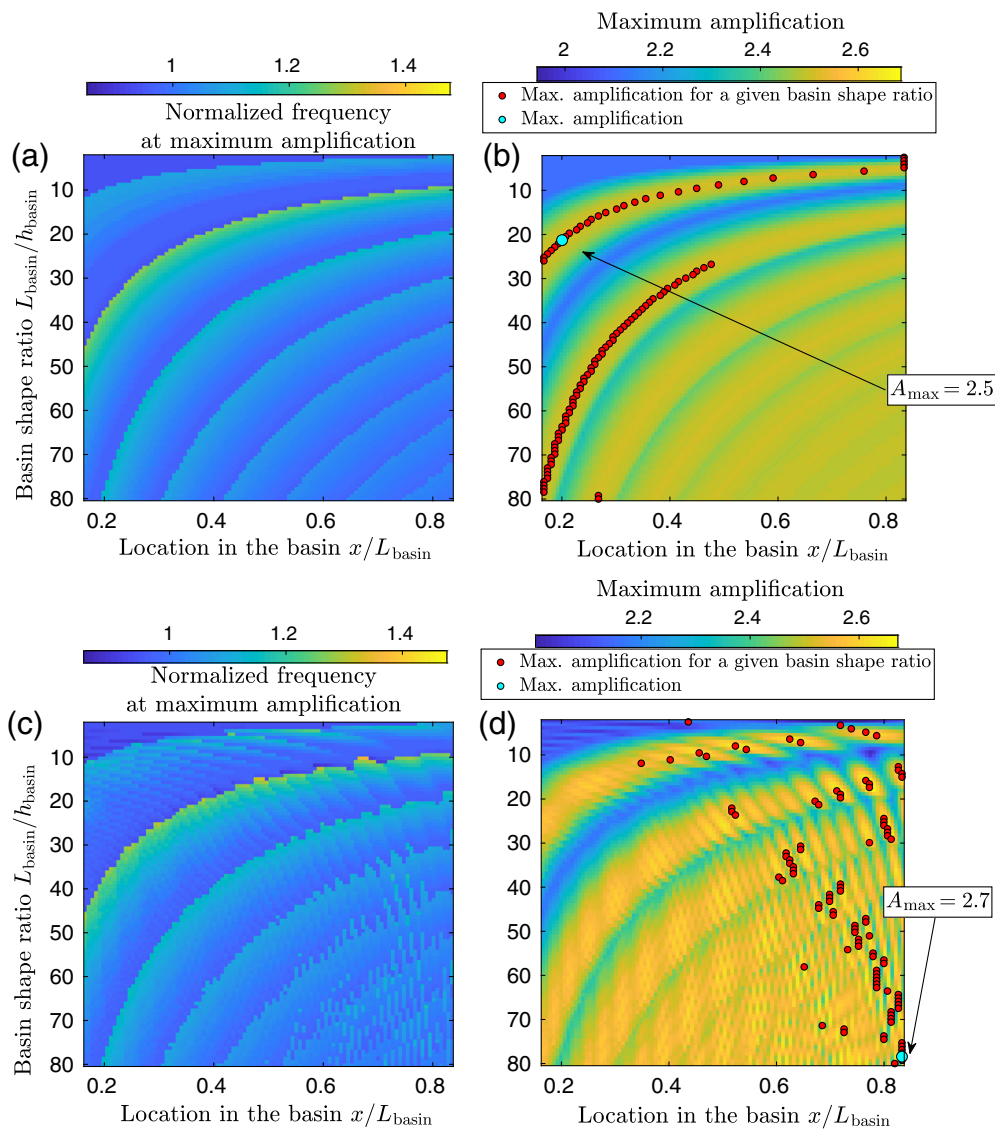
Figure 8. (a,c) Normalized frequency at maximum vertical amplification against relative location in the basin x/L_{basin} and basin-shape ratio L_{basin}/h_{basin} for a given velocity ratio $\frac{V_{S,rock}}{V_{S,basin}} \approx 1.7$ ($V_{0,basin} = 1.2$ km/s and $V_{0,rock} = 2$ km/s) without accounting for reflection (a) within the basin and (c) with reflections. (b,d) Corresponding maximum vertical amplification, computed with equation (5), without accounting for reflection within the basin in (b) and (d) with reflections. Red dots correspond to the relative location of maximum amplification for a given basin-shape ratio. Blue dots correspond to the global maximum amplification. A_{max} is the global maximum amplification value. The color version of this figure is available only in the electronic edition.

Edge slope

The models and comparisons shown thus far assume a purely vertical basin edge. This serves as a "worst case" or especially conservative comparison to 1D theory, and here we consider the effect of relaxing that assumption by varying the angle γ at the basin edge (Fig. 1).

The geometry of a basin is known to have an influence on the spatial distribution of amplification (Narayan *et al.*, 2016; Zhu *et al.*, 2018), with maximum vertical amplification close to the edge of the basin in trapezoidal structures. However, most

studies have focused on the amplification of incident body waves, which inevitably leads to constructive interference between body and diffracted Rayleigh waves, referred to as "the basin-edge effect" (Kawase, 1996). Although this could be significant in particular scenarios, here we are interested in the amplification of incident Rayleigh waves, for which the interaction between diffracted body waves and surface waves should not be the largest contribution to the overall amplification.

The angle γ between the basin edge and the surface will play a crucial role in transmitting or reflecting incident surface waves. As described in equation (3), if the horizontal gradients of the basin edge are small compared to the wavelength, reflections and mode conversions should be negligible (Keilis-Borok, 1989). When γ is small, the amplification should converge to the solution given by the purely 1D theory, because most of the energy is transferred as a fundamental mode. For a vertically incident shear wave, the angle γ has an opposite effect on surface response. For body waves, a small angle γ leads to strong wave conversion at the surface (Narayan *et al.*, 2016). For large basin-edge angles ($\gamma > \pi/3$), Fujii (1986) and Its and Yanovskaya

(1985) concluded that transmission coefficients were only weakly dependent on angle.

The amplification spectra for two different slope angles $\gamma = \pi/20$ and $\pi/2$ as well as the numerical simulations are shown in Figure 11. Specifically, this shows a location 10 km away from the basin edge, defined from the point where the full basin depth is first reached. As we decrease γ, the amplification spectrum converges toward the purely 1D solution, with fewer higher-order mode contributions. Maximum error between the purely 1D and numerical solutions is reached for $\gamma = \pi/2$.
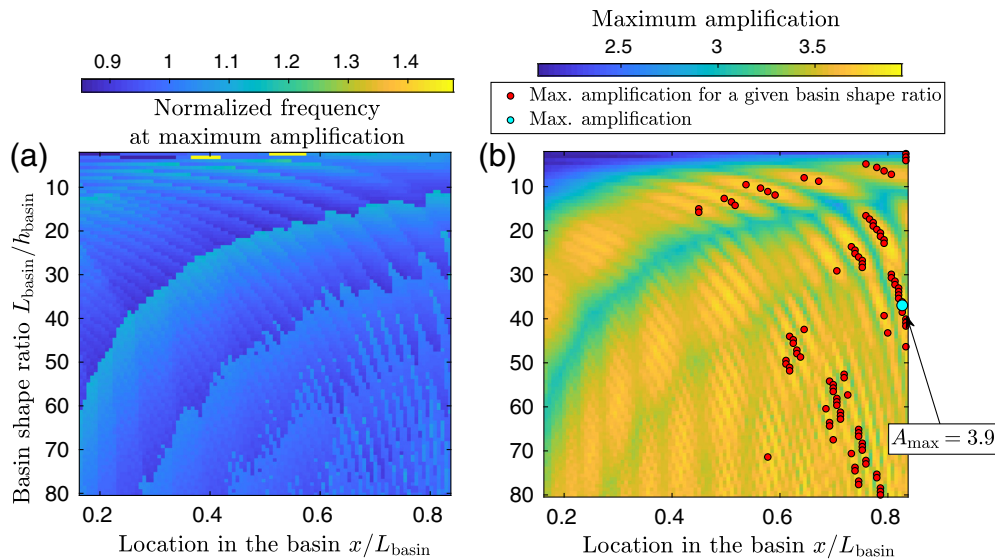
Figure 9. (a) Normalized frequency at maximum vertical amplification against relative location in the basin x/L_{basin} and basin-shape ratio $L_{\text{basin}}/h_{\text{basin}}$ for a given velocity ratio $\frac{V_{S,\text{rock}}}{V_{S,\text{basin}}} = 2$ with reflections. (b) Corresponding maximum vertical amplification, computed with equation (5), against relative location in the basin x/L_{basin} and basin-shape ratio $L_{\text{basin}}/h_{\text{basin}}$. Red dots correspond to the relative location of maximum amplification for a given basin-shape ratio. Blue dots correspond to the global maximum amplification. $A_{\max}$ is the global maximum amplification value. The color version of this figure is available only in the electronic edition.
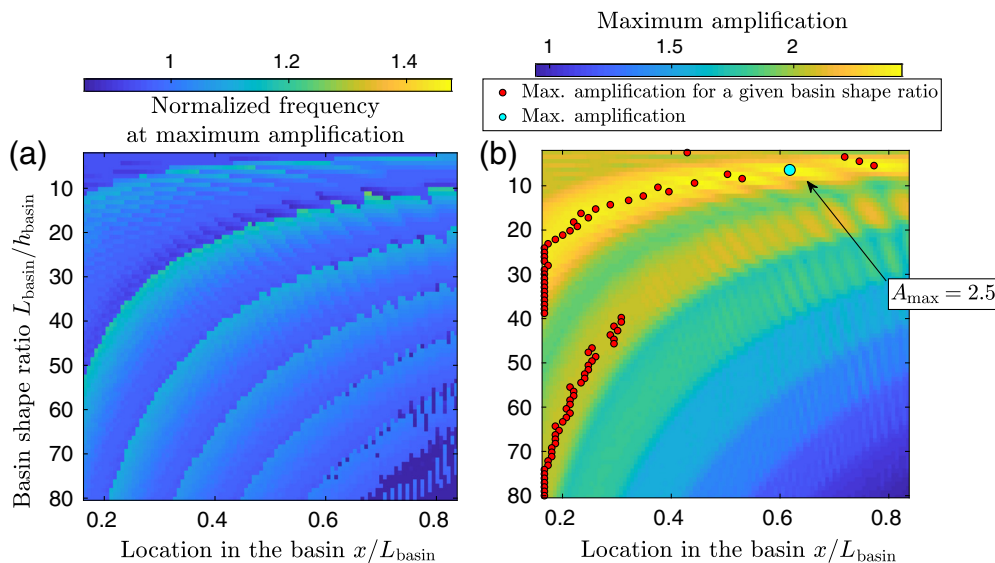

Figure 10. (a) Normalized frequency at maximum vertical amplification against relative location in the basin x/L_{basin} and basin-shape ratio $L_{\text{basin}}/h_{\text{basin}}$ with reflections for a given velocity ratio $\frac{V_{S,\text{rock}}}{V_{S,\text{basin}}} \approx 1.7$ ($V_{0,\text{basin}} = 1.2$ km/s and $V_{0,\text{rock}} = 2$ km/s), $Q_S = 5\%V_{S,\text{basin}}$, with $V_{S,\text{basin}}$ in meters per second, and $Q_P = 2Q_S$. (b) Corresponding maximum vertical amplification, computed with equation (5), including reflections. Red dots correspond to the relative location of maximum amplification for a given basin-shape ratio. Blue dots correspond to the global maximum amplification. $A_{\max}$ is the global maximum amplification value. Scales are different for Figures 8 and 9. The color version of this figure is available only in the electronic edition.

ACCURACY OF THE 1D THEORY FOR MAXIMUM AMPLIFICATION PREDICTIONS

In the previous sections, we observed discrepancies between the 1D theory and a more complete description of amplification that depends on impedance contrast, location, basin depth, and basin length. In this section, we attempt to generalize the conclusions and offer a more complete description regarding these differences.

Accuracy of the purely 1D theory against amplifications computed with transmission coefficients

We first compute the ratio of maximum amplitude of the amplification spectrum derived from the transmission coefficient $A^{\text{1D,trans}}$ over the maximum from the purely 1D theory $A^{\text{1D,pure}}$. We consider this ratio of maximum amplifications for a range of different velocity, impedance, and Poisson's ratio contrasts.

Because the maximum amplitude is location dependent when higher-order modes are considered, we show the geometric mean of the amplification spectra over the first 5 km such that $A^{\text{1D,trans}} = \frac{1}{d}\int_0^d A^{\text{1D,trans}}(x)dx$, in which $d = 5$ km (5 km corresponds roughly to two fundamental-mode wavelengths).

Ratios of maximum amplification from the purely 1D theory over the maximum amplification from the transmission coefficients are presented in Figure 12a,b for three typical Poisson's ratio $\nu = 0.25$, 0.3, 0.35 and constant density $\rho_{\text{basin}} = \rho_{\text{rock}} = 3$ kg/m³. Figure 12a,b
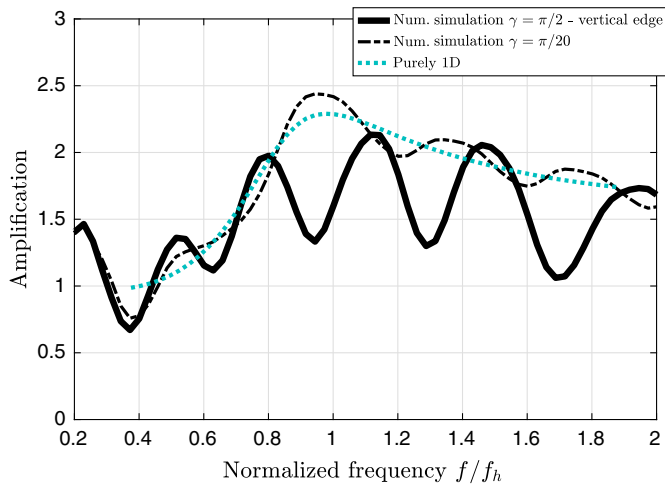
Figure 11. Amplification spectrum against normalized frequency from numerical simulation with slope angle $\gamma = \pi/2$ ("num. simulation $\gamma = \pi/2$ - vertical edge," thick black line) and slope angle $\gamma = \pi/20$ ("num. simulation $\gamma = \pi/20$," black dashed line) and from the purely 1D theory ("purely 1D," blue dashed line) at distance $x = 10$ km from the edge of the basin located at x_a in Figure 1, for $h_{\text{basin}} = 1$ km, $V_{0,\text{basin}} = 1.2$ km/s, and $V_{0,\text{rock}} = 2$ km/s. The color version of this figure is available only in the electronic edition.
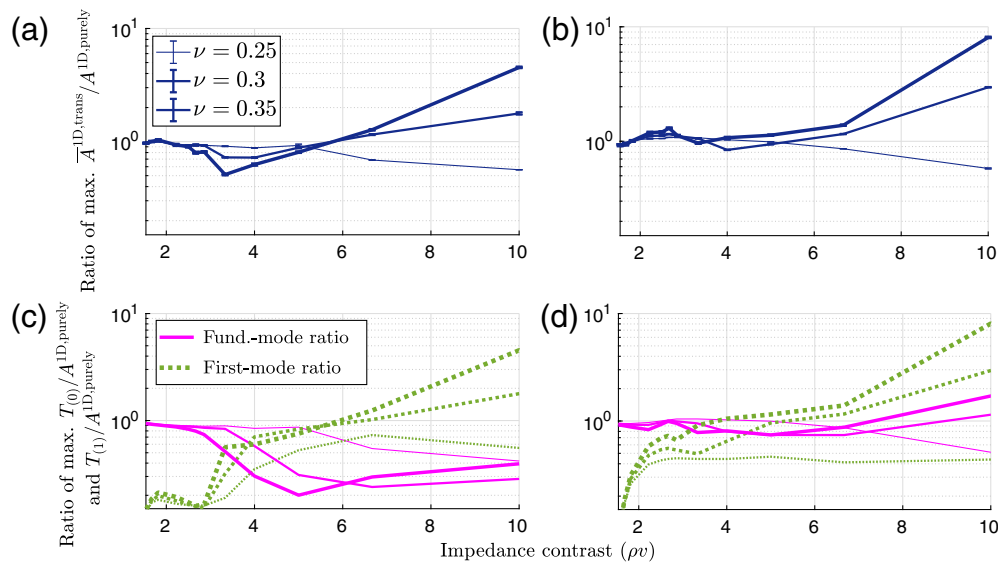
can be interpreted as the ratio of maximum amplitude that has been overpredicted or underpredicted by the 1D theory for a given impedance contrast and a given Poisson's ratio. We show that the ratio for impedance contrasts ranging from 2 to 10, as they are representative of real basins comprising up to 70% of the compiled data from the statistical study by Stambouli et al. (2017). For the vertical component, in Figure 12a, and an impedance contrast $(\rho V_{S,\text{rock}}/\rho V_{S,\text{basin}}) < 6$, the purely 1D theory overpredicts the amplification, consistent with earlier observations in Figures 2 and 3. At higher impedance contrasts, however, the trend reverses, and this can be understood through Figure 12c and d, which show separately the contributions from the fundamental mode and the first overtone. The local minima in the curves from Figure 12a,b, roughly correspond to the points at which the fundamental-to-first conversions start playing a more significant role. The strong mode conversion at the basin boundary may have been the situation, for example, in the Mexico City basin, as presented for the elastic case in Cruz-Atienza et al. (2016).

In contrast to the vertical components, when comparing Figure 12a and b, we observe that the purely 1D theory tends to underpredict the maximum horizontal amplification for an impedance contrast <6. Because of the larger fundamental-to-first higher-order mode transmission coefficient for the horizontal component than for the vertical component, visible in Figure 12d, constructive interference between modes lead to larger maximum amplification not captured by the purely 1D theory. The large horizontal fundamental-to-first higher-order mode conversion is consistent with the conclusions by Narayan (2010, 2012) showing horizontally polarized higher-order modes for low-impedance contrasts. We also include the standard variation (bars around each data point in Fig. 12a,b), because we are averaging observations over the first 5 km. The points of maximum variance occur near the local minima of each curve where both modes contribute equally, and consequently there is more constructive and destructive interference. Though we keep a constant density in these plots for illustrative purposes, a strong density contrast will also play a role in determining how the two modes interact.

Figure 12. (a,b) Ratio of maximum amplification from the purely 1D theory over the maximum amplification from the transmission coefficients for the fundamental and first higher-order mode, averaged over the first 5 km (together with the variance demoted by the error bar), for (a) the vertical component and (b) the horizontal component, against impedance contrast (or velocity contrast since the density is constant) for Poisson's ratio $\nu = 0.25$ (thin), $\nu = 0.3$ (medium), and $\nu = 0.35$ (thick). (c,d) Ratio of maximum amplification from the purely 1D theory over the maximum amplification from the transmission coefficients for the fundamental mode $T_{(0\to0)}$ (pink) and the first higher-order mode $T_{(0\to1)}$ (green dashed line) for (c) the vertical component and (d) the horizontal component against impedance contrast for Poisson's ratio $\nu = 0.25$ (thin), $\nu = 0.3$ (medium), and $\nu = 0.35$ (thick). The color version of this figure is available only in the electronic edition.

TABLE 1
Relative Error in Maximum Amplification between the 1D Theory with Transmission Coefficients and the Simulations

Impedance Contrast $\frac{V_{S,\text{rock}}}{V_{S,\text{basin}}}$	2	5	6.7	10
Vertical relative error in maximum amplification	1%	1%	7.5%	18%
Vertical relative error in dominant frequency	1%	4%	56.5%	
Horizontal relative error in maximum amplification	5%	10%	18%	25%
Horizontal relative error in dominant frequency	5%	9%	10%	11%

Average relative error in maximum amplification in the basin-edge far-field $\frac{\max(A^{1D,\text{trans}})-\max(A^{\text{simu}})}{\max(A^{1D,\text{trans}})}$, in which $A^{1D,\text{trans}}$ is the amplification spectrum from the transmission coefficients for the fundamental and first higher-order mode and A^{simu} is the amplification spectrum from simulation and average relative error in frequency peak in the basin-edge far field for various velocity contrasts $\frac{f_{\max}^{1D,\text{trans}}-f_{\max}^{\text{simu}}}{f_{\max}^{1D,\text{trans}}}$ in which $f_{\max}$ is the frequency at maximum amplification. Results are given for a Poisson's ratio $\nu = 0.25$ and constant density $\rho = 3$ kg m^{-3}.

For impedance contrasts <6, the purely 1D theory leads generally to an overestimation of the vertical amplification and underestimation of the horizontal amplification, and the error remains around 35%. This is less than the epistemic uncertainties sometimes remaining in ground-motion models (GMMs) (Zhu *et al.*, 2018; Kristek *et al.*, 2018), and we believe even the simple parameterizations shown here might reduce overall GMM residuals, if surface waves are taken into account. Thus, for many earthquake hazard estimates, the purely 1D theory may be useful, despite some modest errors.

Accuracy of the transmission coefficients against numerical simulations

Finally, we reiterate again that we have calculated transmission and reflection coefficients by neglecting body-wave contributions in the basin scattered wavefield. This assumption will inevitably lead to an error in the predicted surface energy distribution for large velocity contrasts (Malischewsky, 1976). However, even for extremely large impedance contrasts, both the error in capturing the frequency at maximum amplification and the maximum amplification is less than 18% for the vertical component and less than 25% for the horizontal component, as shown in Table 1, and this discrepancy is usually much smaller. We believe that some, if not most, of this difference comes from unmodeled body-wave conversions at the basin edge, and find that on the whole this contribution to be relatively small for most velocity contrasts. Larger errors in the horizontal amplification are due to the increased contribution of diffracted shear waves at the basin edge compared to the vertical component. This suggests that while accounting for basin edge effects can be important, either through full numerical simulation or the semi-analytic Green's function approach presented here, the 1D theory with added transmission coefficients may also be considered sufficient for many applications.

PREDICTION OF THE AMPLIFICATION SPECTRUM FOR REALISTIC BASIN STRUCTURES

Simple basin geometries and power-law shear-velocity structures enable us to measure the importance of basin parameters in the amplification spectrum, because we can derive an analytic expression for the surface-wave Green's functions. However, realistic basin structures have irregular geometries and more discontinuous velocity profiles, because of the presence of shallow low-velocity sedimentary layers. A remaining question, then, relates to what degree a simple homogeneous basin with a vertical interface can reproduce amplifications in basins of a more realistic geometry.

We continue to focus on the amplification that can be described by our semi-analytic Green's functions, that use only a single basin "box," that is, a vertical boundary on the near edge and far edge of the basin. Here, we use the velocity structure from the Southern California Earthquake Center (SCEC) Community Velocity Model version 4.26 (CVM-S4.26, Lee *et al.*, 2014) for southern California. To compute the transmission coefficients, we first extract a 2D cross section from the Los Angeles basin, as shown in Figure 13, as if a source were originating out toward the San Andreas fault. This model shows a high-velocity contrast $\frac{V_{S,\text{rock}}}{V_{S,\text{basin}}} \approx 4.2$ along an almost vertical boundary, at the location denoted by the black dashed line around $x \approx 64$ km in Figure 13a. We choose a rock-site station around $x \approx 20$ km, where the subsurface is close to homogeneous and a basin station at 15 km from the basin edge because lateral variations of seismic velocities are not too large at that location within the basin. We then build our "box" model (Fig. 13b) using the 1D profile beneath each station to compute the semi-analytic predictions from the purely 1D theory as well as from the transmission coefficients (considering the single boundary defined by the dashed line). Compressional and density profiles are provided in the supplementary material. Finally, we then compare those predictions, based on the box model in Figure 13b, to both the purely 1D theory and to a full 2.5D spectral element simulation based on the full model showed in Figure 13a.

Figure 13b shows three main discontinuities around depths $z_1 = 1.5$ km, $z_2 = 3.8$ km, and $z_3 = 5.2$ km. These discontinuities will affect the basin-amplification spectrum over a limited frequency range that can be derived from estimates of the associated dominant frequencies, similar in the Influence of Basin Structures on Surface-Wave Propagation section. By considering the shear-wave velocity right above each discontinuity, the dominant frequencies defined in equation (6) read
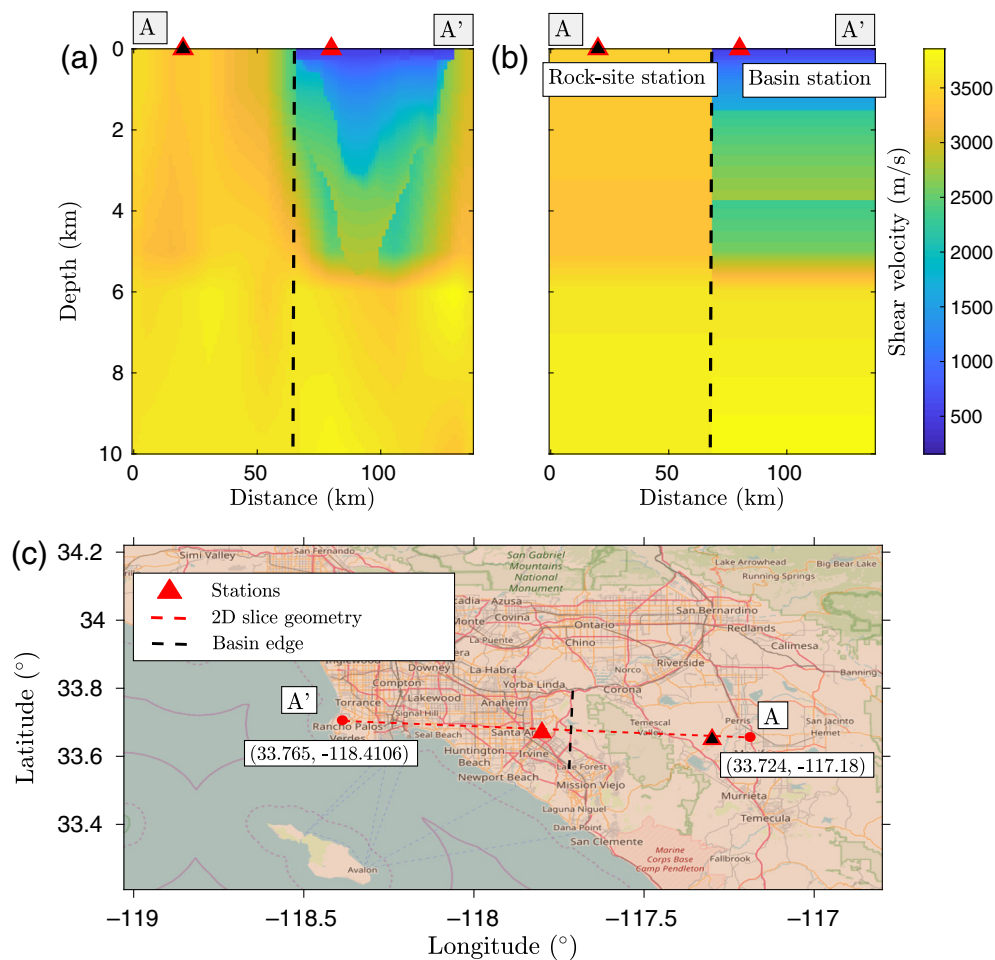
Figure 13. (a) Initial shear-velocity profile extracted from the Southern California Earthquake Center (SCEC) 4.26 model used for the simulation and (b) the corresponding block model used for computing the transmission coefficients. Black and red triangles represent the rock-site and basin stations, respectively. (c) Map of the Los Angeles basin showing the profile geometry extracted to run the simulation which boundaries are denoted by labels A and A′. The color version of this figure is available only in the electronic edition.

and the predictions using the transmission coefficients and numerical methods are dependent on the distance from the basin edge as well as the presence of strong lateral heterogeneities within the basin. To illustrate the impact of lateral heterogeneities we show, in the supplementary material, comparisons further away from the basin edge, at $x = 25$ km, that show stronger discrepancies between predictions using the transmission coefficients and those of the numerical solution. Higher-order modes are generated because of the large lateral shear-velocity variations over the first 20 km within the basin (e.g., discontinuity at depth z_1 presented earlier) that are not captured by the transmission coefficients computed from velocity profiles at $x = 25$ km from the basin edge.

CONCLUSIONS

The purely 1D theory for surface-wave propagation provides a simple way to analytically predict the surface-wave amplification in basin structures (Bowden and Tsai, 2017). However, several strong assumptions are made regarding transmission and conversion of waves at the basin edge. To account for such effects, we use a semi-analytic surface-wave Green's function formulation that can account for a discontinuity between two arbitrary velocity profiles, as described and implemented by Datta (2018). This semi-analytic tool is used to explore a variety of wave propagation effects and to begin to quantify their relative contribution to the total amplification spectrum. All earthquakes are assumed to occur near the surface, with waves propagating laterally into the basin.

We first investigated the discrepancy between the pure 1D theory and the full amplification spectrum in simple basin structures that exhibit strong velocity contrasts. We find that the main reason for this discrepancy is that the 1D theory does not account for coupling between higher-order Rayleigh-wave modes at the basin edge. Higher-order mode transmission coefficient amplitudes become larger than for the fundamental
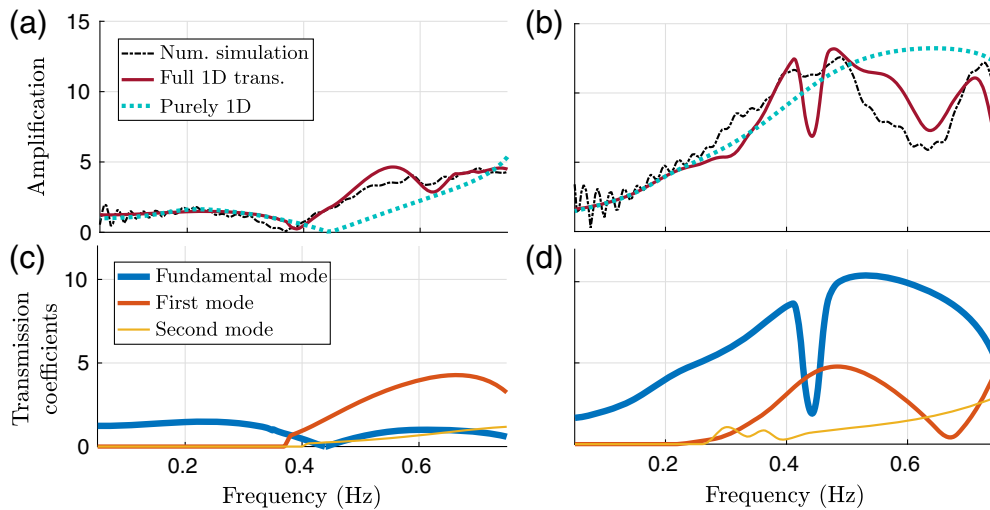
$f_{h,1} \approx 0.5$ Hz, $f_{h,2} \approx 0.32$ Hz, and $f_{h,3} \approx 0.25$ Hz. Therefore, to show the impact of the different discontinuities on the amplification spectrum, we will show results in the frequency range $f = [0.1; 0.75]$ Hz.

Simulation results and analytic predictions are shown in Figure 14. The spectra are given in Figure 14a,b in terms of actual frequencies and not normalized frequencies. Using only the two first higher-order modes, we capture most of the variations of the amplification spectrum even for a highly discontinuous structure. We observe that for frequencies $f < 0.4$ Hz, all three approaches give similar amplification spectra because reflections and higher-order mode conversions are less significant. The horizontal amplification is significantly stronger than the vertical amplification, owing to a strongly horizontally polarized fundamental mode, visible in Figure 14d, which is expected from sedimentary basins (Tanimoto and Rivera, 2005). The discrepancies between the purely 1D prediction

Figure 14. (a,b) Amplification spectra against frequency for (a) the vertical component and (b) the horizontal component from numerical simulation ("num. Simulation," black dashed line), from the 1D transmission coefficients for the fundamental, first higher-order mode, and second higher-order mode ("full 1D trans." thick red line) and from the purely 1D theory ("purely 1D," blue dashed line) for the velocity model showed in Figure 13b. (c,d) Fundamental mode (thick blue line), first higher-order mode (orange), and second higher-order mode (thin yellow) transmission coefficients against frequency for (c) the vertical component and (d) the horizontal component. The color version of this figure is available only in the electronic edition.

mode, specifically when velocity contrasts are greater than four. However, at worst, the discrepancy in maximum amplification remains roughly <35% for the velocity contrasts and Poisson's ratios considered. Other factors such as reflections at basin boundaries, lateral resonance, and basin slope angles play a role in determining the energy distribution to a lesser extent. Moreover, for simple homogeneous basins, the amplification for the vertical component tends to be larger than for the horizontal component at high frequencies ($f > 0.75f_h$) and smaller at lower frequencies ($f < 0.75f_h$). Because of polarity differences between the vertical and the horizontal component, the interaction between the fundamental and higher-order modes can lead to larger frequencies at maximum amplification for the horizontal component than for the vertical component.

The semi-analytic formulation used here—intermode coupling transmission coefficients calculated through displacement and stress continuity equations—provide a remedy to account for reflections and mode conversions at the basin edge. Despite not accounting for diffracted body waves, amplification spectrum amplitudes, and shape are well captured for a large range of velocity contrasts. Moreover, by running simulations in a realistic, complex tomographic model, we find that reducing the problem to a simple vertical boundary between inside and outside the basin can capture the most salient features of the amplification spectrum.

To complete the description of the wave physics in the basin, future studies will focus on nonorthogonal wave incidence leading to Rayleigh-to-Love-wave conversions that are already included in the theory developed by Its (Its and Yanovskaya, 1985), body-wave to surface-wave coupling (Molina-villegas and Jaramillo-fernández, 2018), as well as resonances in 3D structures (Qin et al., 2012; Kamal and Narayan, 2015). We believe that a flexible, efficient, physics-based description of basin effects can be used to provide microzonation estimates of amplification in regions where a fine-scale and fully 3D velocity model is not available or too expensive to produce and run simulations for (similar in goal to work by Panza et al., 2001). The accuracy and efficiency of the tool also provides opportunities for future probabilistic hazard estimates, for which numerous possible earthquake sources must be considered.

DATA AND RESOURCES

ACKNOWLEDGMENTS

REFERENCES

Aki, K. (1993). Local site effects on weak and strong ground motion, Tectonophysics **218,** nos. 1/3, 93–111.

Alsop, L., A. Goodman, and S. Gregersen (1974). Reflection and transmission of inhomogeneous waves with particular application to Rayleigh waves, *Bull. Seismol. Soc. Am.* **64,** no. 6, 1635–1652.

Anderson, D. L., A. Ben-Menahem, and C. B. Archambeau (1965). Attenuation of seismic energy in the upper mantle, *J. Geophys. Res.* **70,** no. 6, 1441–1448.

Bard, P.-Y., and M. Bouchon (1985). The two-dimensional resonance of sediment-filled valleys, *Bull. Seismol. Soc. Am.* **75,** no. 2, 519–541.

Bard, P.-Y., M. Campillo, F. Chavez-Garcia, and F. Sanchez-Sesma (1988). The Mexico earthquake of September 19, 1985A theoretical investigation of large-and small-scale amplification effects in the Mexico City valley, *Earthq. Spectra* **4,** no. 3, 609–633.

Boore, D. M., and W. B. Joyner (1997). Site amplifications for generic rock sites, *Bull. Seismol. Soc. Am.* **87,** no. 2, 327–341.

Borcherdt, R. D. (2014). Implications of next generation attenuation ground motion prediction equations for site coefficients used in earthquake resistant design, *Earthq. Eng. Struct. Dynam.* **43,** no. 9, 1343–1360.

Boué, P., M. Denolle, N. Hirata, S. Nakagawa, and G. C. Beroza (2016). Beyond basin resonance: Characterizing wave propagation using a dense array and the ambient seismic field, *Geophys. J. Int.* **206,** no. 2, 1261–1272.

Bowden, D. C., and V. C. Tsai (2017). Earthquake ground motion amplification for surface waves, *Geophys. Res. Lett.* **44,** no. 1, 121–127.

Brissaud, Q., and V. C. Tsai (2019). Validation of a fast semi-analytic method for surface-wave propagation in layered media, *Geophys. J. Int.* **219,** no. 2, 1405–1420.

Brocher, T. M. (2005). Empirical relations between elastic wavespeeds and density in the earth's crust, *Bull. Seismol. Soc. Am.* **95,** no. 6, 2081–2092.

Chavez-Garcia, F. J., and E. Faccioli (2000). Complex site effects and building codes: Making the leap, *J. Seismol.* **4,** no. 1, 23–40.

Clement, M. J. Y. (1961). The reflection and transmission of Rayleigh waves, *Ph.D. Thesis,* University of British Columbia.

Cruz-Atienza, V. M., J. Tago, J. D. Sanabria-Gómez, E. Chaljub, V. Etienne, J. Virieux, and L. Quintanar (2016). Long duration of ground motion in the Paradigmatic Valley of Mexico, *Sci. Rep.* **6,** 1–9.

Dalton, C. A., and G. Ekström (2006). Global models of surface wave attenuation, *J. Geophys. Res.* **111,** no. B5, 1–19, doi: 10.1029/2005JB003997.

Datta, A. (2018). Swrt: A package for semi-analytical solutions of surface wave propagation, including mode conversion, across transversely aligned vertical discontinuities, *Geosci. Instrum. Methods Data Syst.* **7,** no. 1, 101–112.

De Noyer, J. (1961). The effect of variations in layer thickness on love waves, *Bull. Seismol. Soc. Am.* **51,** no. 2, 227–235.

Du, Z. (2002). Waveform inversion for lateral heterogeneities using multimode surface waves, *Geophys. J. Int.* **149,** no. 2, 300–312.

Fäh, D., P. Suhadolc, S. Mueller, and G. Panza (1994). A hybrid method for the estimation of ground motion in sedimentary basins: Quantitative modeling for Mexico city, *Bull. Seismol. Soc. Am.* **84,** no. 2, 383–399.

Feng, L., and M. H. Ritzwoller (2017). The effect of sedimentary basins on surface waves that pass through them, *Geophys. J. Int.* **211,** no. 1, 572–592.

Field, E. H. (1996). Spectral amplification in a sediment-filled valley exhibiting clear basin-edge-induced waves, *Bull. Seismol. Soc. Am.* **86,** no. 4, 991–1005.

Field, E. H. (2000). Accounting for site effects in probabilistic seismic hazard analyses of southern California: Overview of the SCEC phase III report, *Bull. Seismol. Soc. Am.* **90,** no. 6B, S1–S31.

Fujii, K. (1986). The scattering of Rayleigh waves at a variously inclined discontinuity, *J. Phys. Earth* **34,** no. 6, 487–515.

Graves, R., T. H. Jordan, S. Callaghan, E. Deelman, E. Field, G. Juve, C. Kesselman, P. Maechling, G. Mehta, K. Milner, et al. (2010). CyberShake: A physics-based seismic hazard model for Southern California, *Pure Appl. Geophys.* **168,** nos. 3/4, 367–381.

Graves, R. W., and A. Pitarka (2010). Broadband ground-motion simulation using a hybrid approach, *Bull. Seismol. Soc. Am.* **100,** no. 5A, 2095–2123.

Hanks, T. C. (1975). Strong ground motion of the San Fernando, California, earthquake: Ground displacements, *Bull. Seismol. Soc. Am.* **65,** no. 1, 193–225.

Haskell, N. A. (1962). Crustal reflection of plane P and SV waves, *J. Geophys. Res.* **67,** no. 12, 4751–4768.

Hauksson, E., and P. M. Shearer (2006). Attenuation models (Q_P and Q_S) in three dimensions of the southern California crust: Inferred fluid saturation at seismogenic depths, *J. Geophys. Res.* **111,** no. B5, 1–21, doi: 10.1029/2005JB003947.

Hauksson, E., T.-L. Teng, and T. L. Henyey (1987). Results from a 1500 m deep, three-level downhole seismometer array: Site response, low q values, and f max, *Bull. Seismol. Soc. Am.* **77,** no. 6, 1883–1904.

Its, E., and T. Yanovskaya (1985). Propagation of surface waves in a half-space with vertical, inclined or curved interfaces, *Wave Motion* **7,** no. 1, 79–94.

Kamal, B., and J. P. Narayan (2015). 3d basin-shape ratio effects on frequency content and spectral amplitudes of basin-generated surface waves and associated spatial ground motion amplification and differential ground motion, *J. Seismol.* **19,** no. 2, 293–316.

Kawase, H. (1996). The cause of the damage belt in Kobe: "The basin-edge effect," constructive interference of the direct s-wave with the basin-induced diffracted/Rayleigh waves, *Seismol. Res. Lett.* **67,** no. 5, 25–34.

Kawase, H. (2003). Site effects on strong ground motions, *Int. Geophys. Ser.* **81,** no. B, 1013–1030.

Keilis-Borok, V. I. (1989). Surface waves in media with weak lateral inhomogeneity, in *Seismic Surface Waves in a Laterally Inhomogeneous Earth,* V. I. Keilis-Borok and A. L. Levshin (Editors), Kluwer Academic Publishers, Dordrecht, The Netherlands, 35–69.

Koketsu, K., H. Miyake, H. Fujiwara, and T. Hashimoto (2008). Progress towards a Japan integrated velocity structure model and long-period ground motion hazard map, *Proc. of the 14th World Conf. on Earthquake Engineering,* S10–038.

Komatitsch, D., and J.-P. Vilotte (1998). The spectral element method: An efficient tool to simulate the seismic response of 2d and 3d geological structures, *Bull. Seismol. Soc. Am.* **88,** no. 2, 368–392.

Kristek, J., P. Moczo, P.-Y. Bard, F. Hollender, and S. Stripajová (2018). Computation of amplification factor of earthquake ground motion for a local sedimentary structure, *Bull. Earthq. Eng.* **16,** no. 6, 2451–2475.

Lee, E.-J., P. Chen, T. H. Jordan, P. B. Maechling, M. A. Denolle, and G. C. Beroza (2014). Full-3-d tomography for crustal structure in southern California based on the scattering-integral and the adjoint-wavefield methods, *J. Geophys. Res.* **119,** no. 8, 6421–6451.

Lin, F.-C., V. C. Tsai, and M. H. Ritzwoller (2012). The local amplification of surface waves: A new observable to constrain elastic velocities, density, and anelastic attenuation, *J. Geophys. Res.* **117,** no. B6, 1–20, doi: 10.1029/2012JB009208.

Liu, K., and Y. Zhou (2016). Travelling-wave green tensor and near-field Rayleigh-wave sensitivity, *Geophys. Suppl. Mon. Not. Roy. Astron. Soc.* **205,** no. 1, 134–145.

Lontsi, A. M., F. J. Sánchez-Sesma, J. C. Molina-Villegas, M. Ohrnberger, and F. Krüger (2015). Full microtremor H/V (z, f) inversion for shallow subsurface characterization, *Geophys. J. Int.* **202,** no. 1, 298–312.

Malischewsky, P. (1976). Surface waves in media having lateral inhomogeneities, *Pure Appl. Geophys.* **114,** no. 5, 833–843.

Marafi, N. A., M. O. Eberhard, J. W. Berman, E. A. Wirth, and A. D. Frankel (2017). Effects of deep basins on structural collapse during large subduction earthquakes, *Earthq. Spectra* **33,** no. 3, 963–997.

Marquering, H., and R. Snieder (1995). Surface-wave mode coupling for efficient forward modelling and inversion of body-wave phases, *Geophys. J. Int.* **120,** no. 1, 186–208.

Maupin, V., and B. Kennett (1987). On the use of truncated modal expansions in laterally varying media, *Geophys. J. Roy. Astron. Soc.* **91,** no. 3, 837–851.

Meier, T., and P. Malischewsky (2000). Approximation of surface wave mode conversion at a passive continental margin by a mode-matching technique, *Geophys. J. Int.* **141,** no. 1, 12–24.

Meier, T., P. Malischewsky, and H. Neunhöfer (1997). Reflection and transmission of surface waves at a vertical discontinuity and imaging of lateral heterogeneity using reflected fundamental Rayleigh waves, *Bull. Seismol. Soc. Am.* **87,** no. 6, 1648–1661.

Moczo, P., J. Kristek, P.-Y. Bard, S. Stripajová, F. Hollender, Z. Chovanová, M. Kristeková, and D. Sicilia (2018). Key structural parameters affecting earthquake ground motion in 2d and 3d sedimentary structures, *Bull. Earthq. Eng.* **16,** no. 6, 2421–2450.

Molina-villegas, J. C., and J. D. Jaramillo-fernández (2018). Local generation of Love surface waves at the edge of a 2D Alluvial Valley, *Bull. Seismol. Soc. Am.* **XX,** no. Xx, 1–14.

Narayan, J. P. (2005). Study of basin-edge effects on the ground motion characteristics using 2.5-d modelling, *Pure Appl. Geophys.* **162,** no. 2, 273–289.

Narayan, J. P. (2010). Effects of impedance contrast and soil thickness on basin-transduced Rayleigh waves and associated differential ground motion, *Pure Appl. Geophys.* **167,** no. 12, 1485–1510.

Narayan, J. P. (2012). Effects of P-wave and S-wave impedance contrast on the characteristics of basin transduced Rayleigh waves, *Pure Appl. Geophys.* **169,** no. 4, 693–709.

Narayan, J. P., and S. P. Singh (2006). Effects of soil layering on the characteristics of basin-edge induced surface waves and differential ground motion, *J. Earthq. Eng.* **10,** no. 04, 595–614.

Narayan, J. P., P. K. Singh, and Kamal (2016). Effects of basin parameters on the spatial variation of characteristics of basin generated Rayleigh waves, *Int. J. Geo-Eng.* **7,** no. 1, 17.

Olsen, K. (2000). Site amplification in the Los Angeles basin from three-dimensional modeling of ground motion, *Bull. Seismol. Soc. Am.* **90,** no. 6B, S77–S94.

Panza, G. F., F. Romanelli, and F. Vaccari (2001). Seismic wave propagation in laterally heterogeneous anelastic media: Theory and applications to seismic zonation, *Adv. Geophys.* **43,** 1–95, doi: 10.1016/S0065-2687(01)80002-9.

Pratt, T. L., T. M. Brocher, C. S. Weaver, K. C. Creager, C. M. Snelson, R. S. Crosson, K. C. Miller, and A. M. Tréhu (2003). Amplification of seismic waves by the Seattle basin, Washington state, *Bull. Seismol. Soc. Am.* **93,** no. 2, 533–545.

Qin, Y., Y. Wang, H. Takenaka, and X. Zhang (2012). Seismic ground motion amplification in a 3d sedimentary basin: The effect of the vertical velocity gradient, *J. Geophys. Eng.* **9,** no. 6, 761.

Romanelli, F., J. Bekkevold, and G. Panza (1997). Analytical computation of coupling coefficients in non-poissonian media, *Geophys. J. Int.* **129,** no. 1, 205–208.

Sanchez-Sesma, F. J., and F. Luzon (1995). Seismic response of three-dimensional alluvial valleys for incident P, S, and Rayleigh waves, *Bull. Seismol. Soc. Am.* **85,** no. 1, 269–284.

Sánchez-Sesma, F. J., and S. A. Velázquez (1987). On the seismic response of a dipping layer, *Wave Motion* **9,** no. 5, 387–391.

Savage, B., and D. Helmberger (2004). Complex Rayleigh waves resulting from deep sedimentary basins, *Earth Planet. Sci. Lett.* **218,** nos. 1/2, 229–239.

Stambouli, A. B., D. Zendagui, P.-Y. Bard, and B. Derras (2017). Deriving amplification factors from simple site parameters using generalized regression neural networks: Implications for relevant site proxies, *Earth Planets Space* **69,** no. 1, 99.

Tamura, S. (1996). Comparison of body and Rayleigh wave displacements generated by a vertical point force on a layered elastic medium, *Proc. 11th World Conf. Earthquake Engineering*, Acapulco, Mexico, 23–28 June 1996.

Tanimoto, T., and L. Rivera (2005). Prograde Rayleigh wave particle motion, *Geophys. J. Int.* **162,** no. 2, 399–405.

Thompson, E. M., L. G. Baise, R. E. Kayen, and B. B. Guzina (2009). Impediments to predicting site response: Seismic property estimation and modeling simplifications, *Bull. Seismol. Soc. Am.* **99,** no. 5, 2927–2949.

Tromp, J., and F. Dahlen (1992). Variational principles for surface wave propagation on a laterally heterogeneous earth—II. Frequency-domain JWKB theory, *Geophys. J. Int.* **109,** no. 3, 599–619.

Tuan, T. T., F. Scherbaum, and P. G. Malischewsky (2011). On the relationship of peaks and troughs of the ellipticity (H/V) of Rayleigh waves and the transmission response of single layer over half-space models, *Geophys. J. Int.* **2,** no. 184, 793–800.

Zhu, C., D. Thambiratnam, and C. Gallage (2018). Statistical analysis of the additional amplification in deep basins relative to the 1d approach, *Soil Dynam. Earthq. Eng.* **104,** 296–306.